

## Predictability Studies of the Intraseasonal Oscillation with the ECHAM5 GCM

STEFAN LIESS

*Institute for Terrestrial and Planetary Atmospheres, The University at Stony Brook, State University of New York,  
Stony Brook, New York*

DUANE E. WALISER

*Jet Propulsion Laboratory, Pasadena, California*

SIEGFRIED D. SCHUBERT

*NASA Goddard Space Flight Center, Greenbelt, Maryland*

(Manuscript submitted 21 September 2004, in final form 21 February 2005)

### ABSTRACT

Our ability to predict active and break periods of the Asian summer monsoon is intimately tied to our ability to predict the intraseasonal oscillation (ISO). The present study analyzes the upper limit of potential predictability of the northern summer ISO, as it is simulated by the ECHAM5 atmospheric general circulation model forced with climatological SSTs. The leading extended empirical orthogonal functions of precipitation, computed from a 10-yr control simulation, are used to define four different phases of the ISO. Fourteen-member ensembles of 90-day hindcasts are run for each phase of the three strongest ISO events identified in the 10-yr control run. Initial conditions for each ensemble are created from the control simulation using a breeding method.

The signal-to-noise ratio is analyzed over a region that covers the core of the Asian summer monsoon activity. Over Southeast Asia, the upper limit for predictability of precipitation and 200-hPa zonal wind is about 27 and 33 days, respectively. Over India, values of more than 15 days occur for both variables. A spatial analysis of the different phases of the ISO reveals that the predictability follows the eastward- and northward-propagating ISO during the active and break phases of the monsoon. Precipitation reveals increased predictability at the end of the convective phase. Analogous, 200-hPa zonal wind shows strongest predictability during low and easterly anomalies. This potential predictability is considerably higher than for numerical forecasts of typical weather variations, particularly for the Tropics, indicating that useful forecasts of monsoon active and break events may be possible with lead times of more than two weeks for precipitation and the dynamics. A closer look at the breeding method used here to initialize the hindcasts shows the importance of appropriate ensemble experiment designs.

### 1. Introduction

The useful prediction of typical weather phenomena is currently confined to 6–10 days (e.g., Lorenz 1965, 1982; Van den Dool 1994). However, a longer range of predictability is expected for larger-scale climate features with longer periods. The likely limit of predictability for the El Niño–Southern Oscillation (ENSO) for example is currently on the order of 12 to 18 months

(e.g., Cane et al. 1986; Barnston et al. 1994; Graham and Barnett 1995; Barnston et al. 1999). However, the prediction of interannual variations of the Asian summer monsoon provides an ongoing challenge for numerical weather forecasts. Sperber et al. (2001) found in a multimodel study with seven models and between four and nine ensemble forecasts per model that only the first empirical orthogonal function (EOF), associated with the tropical convergence zone being located over the continental landmass, is reasonably predicted by most general circulation models (GCM).

In addition to the Asian–Australian monsoon circulation and ENSO, the intraseasonal oscillation (ISO), also known as Madden–Julian oscillation (Madden and

---

*Corresponding author address:* Stefan Liess, Institute for Terrestrial and Planetary Atmospheres, The University at Stony Brook, State University of New York, Stony Brook, NY 11794-5000.  
E-mail: stefan.liess@stonybrook.edu

Julian 1994), has become an important topic in tropical meteorology. The ISO is largely responsible for the onset of active and break events of the Asian–Australian monsoon system (e.g., Hendon and Liebmann 1990a,b; Lau et al. 1998; Waliser et al. 2003a) during summer in the respective hemisphere. During the Asian summer monsoon, the propagation of the ISO is shifted north-eastward so that its influence could reach as far north as to northern India and the Himalayan Mountains (Yasunari 1980, 1981). Other studies (e.g., McPhaden and Taft 1988; Kessler et al. 1995; Hendon et al. 1998) point out the relationship of the eastward propagation of convective anomalies over the equatorial western Pacific Ocean to the modification of the thermocline in the eastern Pacific Ocean, particularly in Northern Hemisphere winter. Among others, Weickmann (1991) and Kessler and Kleeman (2000) stated that this modification could trigger variations in ENSO. Remote influences of the ISO include the development of persistent North Pacific circulation anomalies during Northern Hemisphere winter (e.g., Ferranti et al. 1990). Also the rainfall variability along the western United States has been linked to the longitudinal position of the convective anomalies associated with the ISO (e.g., Mo and Higgins 1998b,a; Jones 2000; Higgins et al. 2000), especially during Northern Hemisphere summer (Maloney and Hartmann 2000; Higgins and Shi 2001). Analogous studies for the Southern Hemisphere (e.g., Paegle et al. 2000) found a link between the rainfall variability over the Pacific–South American sector and the ISO during the Southern Hemisphere summer.

Based on the above connections between the ISO and other weather and climate features, particularly the Asian summer monsoon, the present study focuses on the predictability of the Northern Hemisphere summer ISO. Thus far, statistical models have shown predictive skill of 15–20 days for the ISO (e.g., Waliser et al. 1999a; Wheeler and Weickmann 2001; Mo 2001). Currently, the India Meteorological Department utilizes statistical models for the monsoon forecast (e.g., Del-Sole and Shukla 2002). Since these models are limited in their ability to reproduce actual weather and other important climate phenomena, GCM forecasts have been analyzed for their ability to predict the ISO. For example, Chen and Alpert (1990), Waliser et al. (1999a), Jones et al. (2000), and Hendon et al. (2000) found an ISO forecast skill of less than 7 days in the National Centers for Environmental Prediction (NCEP) Medium-Range Forecast (MRF) model's Dynamic Extended Range Forecast (DERF). A model intercomparison by Slingo et al. (1996) found a relatively weak ISO signature in the National Meteorological Center (NMC) model, which is a predecessor of the

MRF DERF, compared to other GCMs. The Goddard Laboratory for the Atmospheres (GLA) GCM was among the models that generated a more realistic ISO.

A realistic representation of the ISO is a crucial factor for a predictability study within the intraseasonal time scale. Waliser et al. (2003c) used the GLA GCM to analyze the ISO predictability during Northern Hemisphere summer. They found an extended predictability for the ISO of about 30 days for 30–90-day band-pass-filtered 200-hPa velocity potential anomalies and about 18 days for precipitation anomalies associated with the ISO, although they pointed out some caveats of the GLA GCM, for example, over the Indian Ocean less variability of precipitation is associated with the ISO than in observations; the GLA GCM has a relatively low resolution of  $4^\circ$  latitude  $\times$   $5^\circ$  longitude and 17 vertical layers. These caveats, and the fact that analyses with different models could lead to different results, motivate the present study to focus on the ISO simulation with the ECHAM GCM. Kemball-Cook et al. (2002) found a reasonably well-simulated Northern Hemisphere summer ISO in the ECHAM model. Another improvement of the present study is the use of the breeding method (Toth and Kalnay 1993) to generate perturbations for the initial conditions of the ensemble experiments, which result in fast-growing error modes and thus cover a broad range of forecast values.

The changes from the ECHAM4 version used by Kemball-Cook et al. (2002) to the ECHAM5 model utilized in this study and the experimental framework are presented in section 2. Section 3 provides the results of this predictability study and section 4 gives a brief summary of the present findings.

## 2. Experimental framework

The spectral ECHAM5 GCM is described in detail by Roeckner et al. (2003). The prognostic variables are vorticity, divergence, logarithm of surface pressure, temperature, specific humidity, and the mixing ratio of total cloud water. The ECHAM5 model utilizes the semi-Lagrangian advection scheme by Lin and Johnson (1996), whereas in ECHAM4 the advection scheme by Williamson and Rasch (1994) was used. Other new features include the usage of a prognostic–statistical scheme for the total water content (Tompkins 2002). The standard resolution of the GCM is increased from T42 (corresponding to  $2.8125^\circ \times 2.8125^\circ$ ) with 19 vertical layers in ECHAM4 to T63 (corresponding to  $1.875^\circ \times 1.875^\circ$ ) with 19, and optionally 31, vertical layers in ECHAM5. The vertical domain is confined to 10 hPa in both vertical resolutions. In this study, the T63 resolution with 31 vertical layers is chosen since

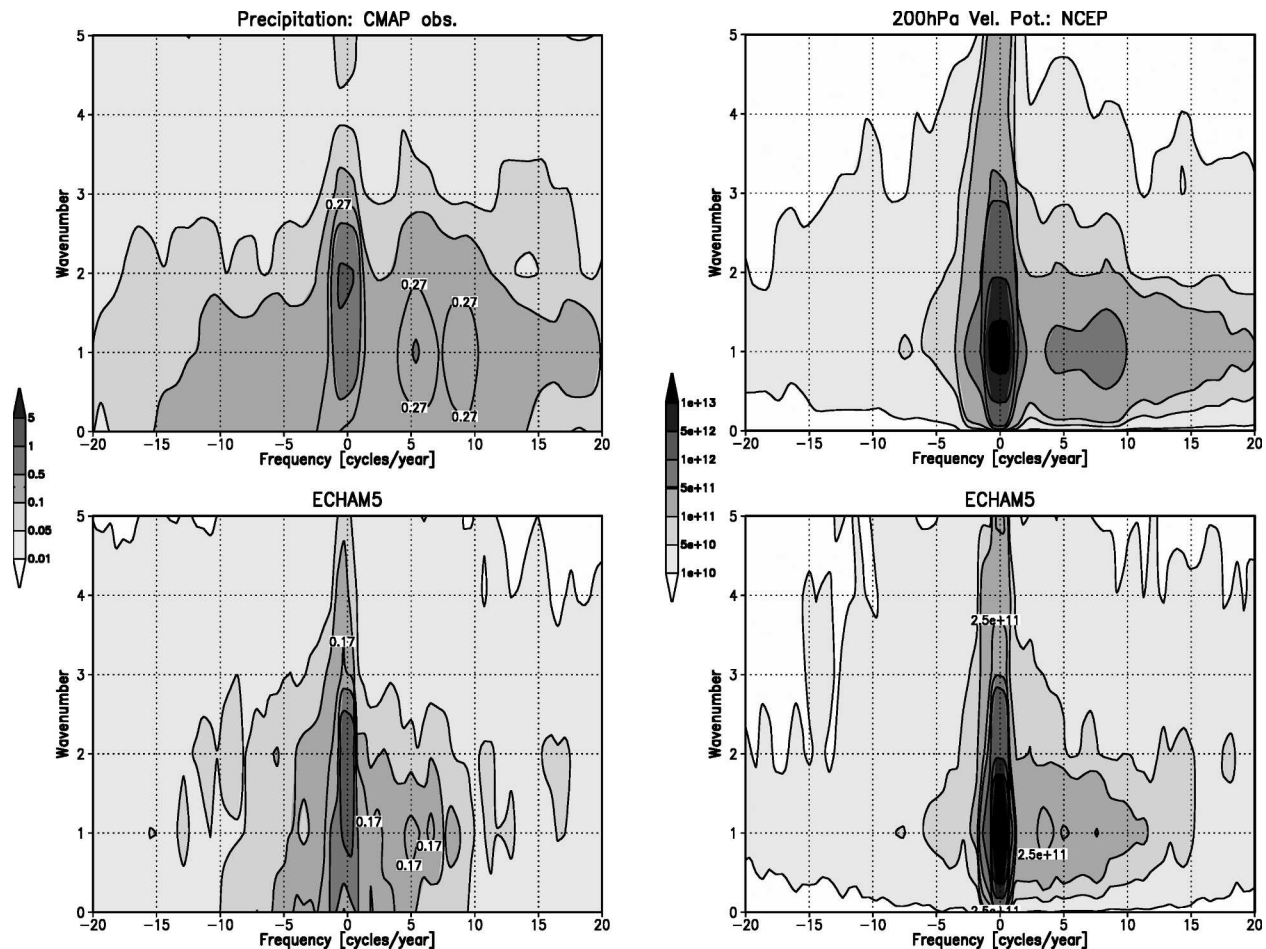


FIG. 1. Zonal wavenumber–frequency spectra of (left) precipitation and (right) 200-hPa zonal wind averaged from  $5^{\circ}\text{N}$  to  $5^{\circ}\text{S}$ . (top) Observations and reanalysis data, and (bottom) model results. Positive (negative) frequencies indicate eastward (westward) propagation.

Inness et al. (2001) and Liess and Bengtsson (2004) found an improved simulation of the midlevel convection and thus the ISO due to increased vertical resolution.

The present study analyzes the predictability of the Northern Hemisphere summer ISO, as it is simulated by the ECHAM5 GCM. The GCM is forced with climatological SSTs in order to eliminate the influence of the ENSO cycle. The model is integrated for 11 yr with the first year discarded to avoid influences by the model spinup. This simulation is referred to as the control experiment.

Daily averaged data of precipitation and 200-hPa velocity potential from the remaining 10 model years are used to validate the simulated ISO with 10 years (1988–1997) of NCEP reanalysis and Climate Prediction Center (CPC) Merged Analysis of Precipitation (CMAP) observations (Xie and Arkin 1997). CMAP data are available as 5-day averages (pentads) only. Wavenum-

ber–frequency spectra averaged over the equatorial region from  $5^{\circ}\text{N}$  to  $5^{\circ}\text{S}$  (Fig. 1) are calculated according to Hayashi (1981). Negative (positive) frequencies denote westward (eastward) propagation. The peaks between  $-1$  and  $+1$  cycles per year describe the annual means and annual cycles, which are not removed from these data. CMAP precipitation and NCEP 200-hPa velocity potential clearly show the eastward propagating ISO with peaks between 5 and 10 cycles per year. The simulated ISO is weaker and slightly slower but still detectable in the unfiltered data. The northward propagation of the precipitation pattern can be analyzed in the meridional wavenumber–frequency spectra from  $25^{\circ}\text{N}$  to  $10^{\circ}\text{S}$  averaged between  $60^{\circ}\text{E}$  and  $180^{\circ}$  (Fig. 2). Again, the simulated oscillation of about eight cycles per year is weaker but still detectable.

To identify regional characteristics, Fig. 3 shows composites of the 30–90-day bandpass-filtered spatiotemporal pattern of precipitation for observations on the

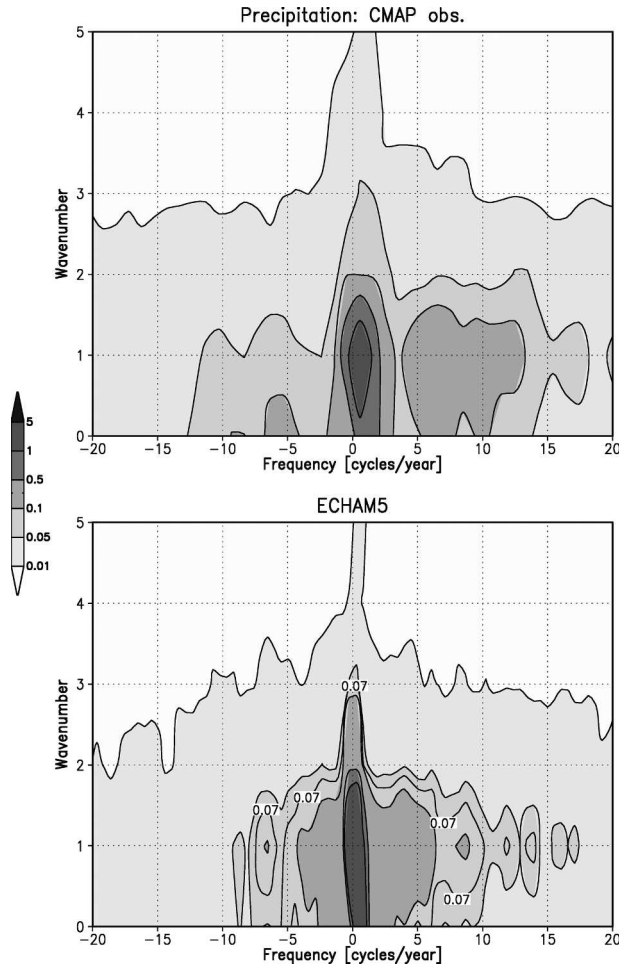


FIG. 2. Meridional wavenumber–frequency spectra of precipitation between 25°N and 10°S averaged from 60°E to 180°: (top) CMAP observations and (bottom) model results. Positive (negative) frequencies indicate northward (southward) propagation.

left and for the ECHAM5 simulation on the right for pentad average values of Northern Hemisphere summer (May–October) over the region 31.25°N to 31.25°S, 50°E to 180°. Most of the boreal summer ISO variability is found in this region (e.g., Wang and Rui 1990) and a connection to the Asian summer monsoon rainfall is apparent (Kang et al. 2002). A 30–90-day Lanczos filter (Duchon 1979) is applied to isolate the ISO signal in the data. The total filter length is 150 days. Extended EOFs (EEOFs) over the above domain are calculated with the extended time dimension ranging from –5 to +5 pentads.

The composites are created from the associated first EEOF and include all pentads that have an amplitude greater than 0.8 in the normalized principal component time series (see the top of Fig. 5 for the ECHAM5 time series), analogous to the analysis by Waliser et al. (2003c).

The composites consist of 24 (20) events for the observations (ECHAM5). For a concise intercomparison and compact illustration two successive pentads are averaged together and renamed with their averaged number, beginning with pentad –5 and pentad –4 averaged to pentad –4.5 and ending with pentad +3 and pentad +4 averaged to pentad +3.5. The observed ISO cycle begins with the onset of a break event during the summer monsoon. The strongest precipitation is found over the west Pacific warm pool and the Philippines. At pentad –2.5, deep convection forms over the equatorial Indian Ocean and the negative precipitation anomaly moves northward with a northwest tilted shape. At pentad –0.5, the precipitation of the growing convection cell reaches southern India. The monsoon precipitation spreads out over central India at pentad +1.5 and the northwest tilt in the precipitation pattern is detectable. Pentad +3.5 resembles pentad –4.5; thus the period of the northward propagation is about 40 days, as previously observed by Yasunari (1981). The first EEOF of the simulation is nearly in phase with that of the observations. In addition to the eastward shift of the precipitation pattern, the bimodal southwest–northeast structure is not as clear as in the observations. Figure 3 also shows that the GCM fails to reproduce consistent large-scale cloud clusters and thus the cohesive characteristic of the observed precipitation pattern. A realistic representation of precipitation is dependent on various GCM components including the convection scheme and the parameterization of cloud cover. Raymond (2000) and Tompkins (2002) point out general uncertainties related to the parameterization of cloud–radiative feedback. The present analysis is similar to an intercomparison of 10 GCMs in Fig. 7 of Waliser et al. (2003a) and while not in their study, ECHAM5 shows relatively realistic results.

The composite cycle of the 200-hPa velocity potential (Fig. 4) is created from the principal component of EEOFs of the precipitation data. It starts with a positive anomaly over the central Indian Ocean during pentad –4.5, indicating large-scale sinking motion. Please note that the whole Tropics are shown due to the global characteristics of the velocity potential. While the NCEP reanalysis shows a single peak over the central Indian Ocean, the simulation contains a bimodal structure with one peak over the central Indian Ocean and the other already farther eastward over the west Pacific warm pool, which is coherent to the simulated negative precipitation anomalies at pentad –4.5 in Fig. 3. At pentad –2.5, the positive 200-hPa velocity potential anomaly extends over most of the west Pacific warm pool with a lower amplitude in the model. A negative velocity potential anomaly develops over tropical Af-

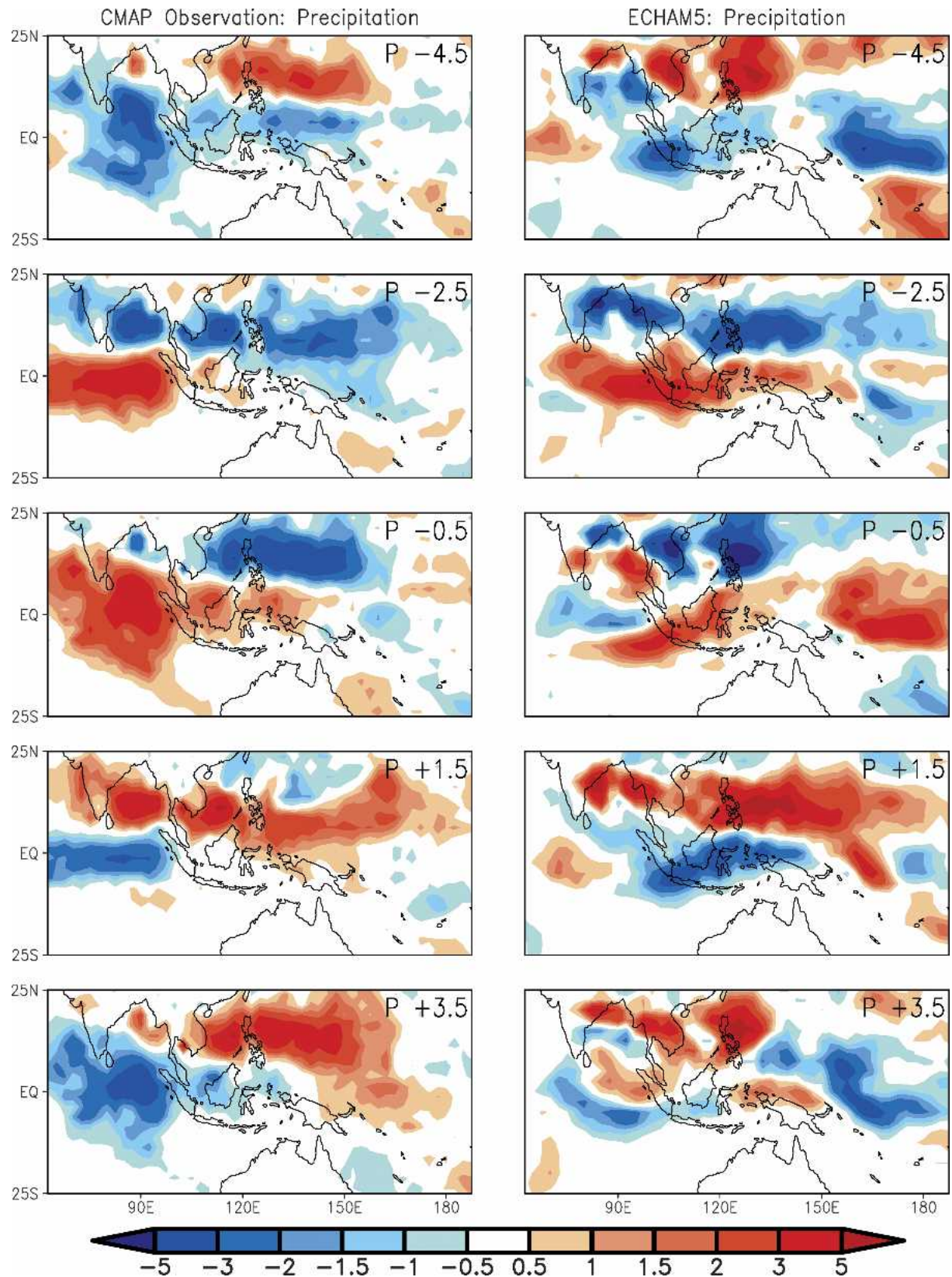


FIG. 3. Precipitation composites ( $\text{mm day}^{-1}$ ) of (left) CMAP observations and (right) ECHAM5 simulations. Segments are separated by 10 days with time increasing from top to bottom. Each map is an average of the two adjacent pentad composites starting with pentad  $-5$  and ending with pentad  $+4$  (see text for more explanations).

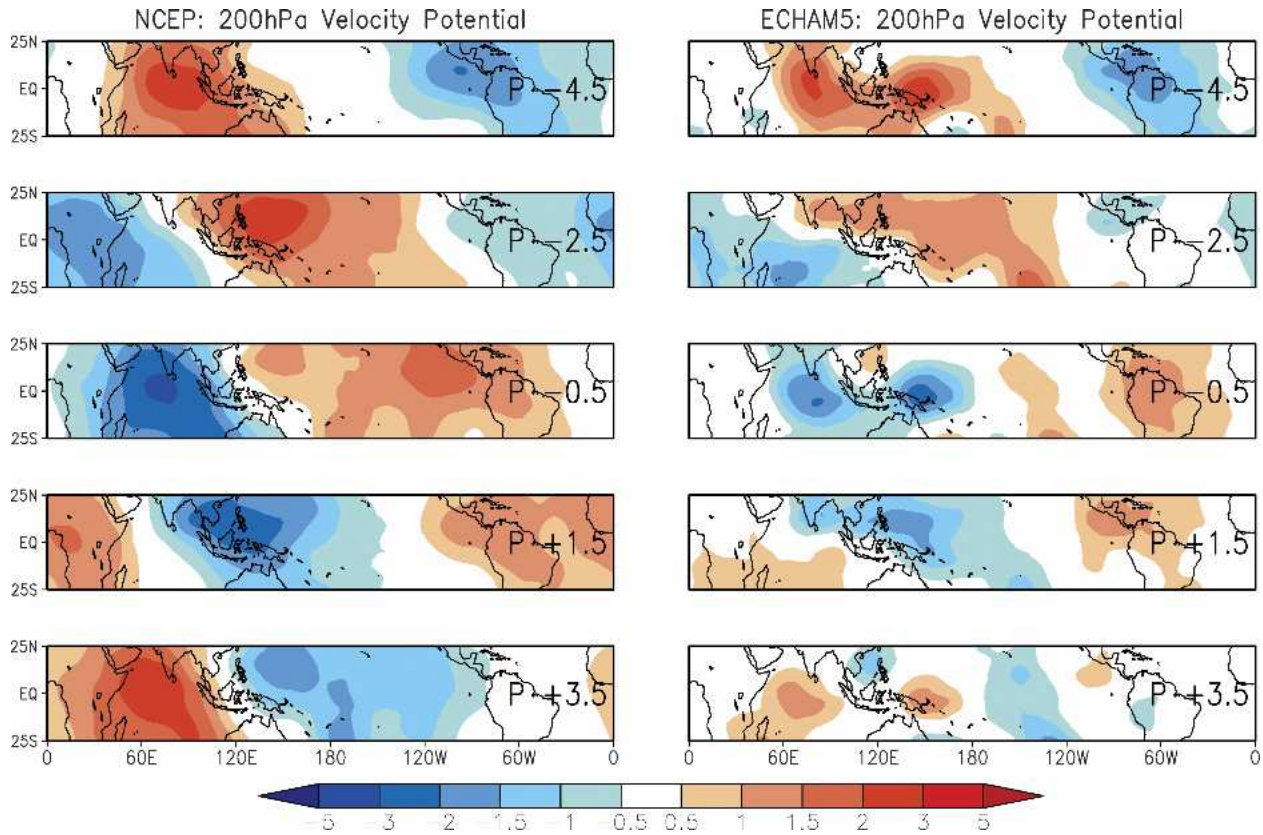


FIG. 4. As in Fig. 3 but for 200-hPa velocity potential ( $10^6 \text{ m}^2 \text{ s}^{-1}$ ) from (left) NCEP reanalysis and (right) ECHAM5 simulation.

rica. At pentad  $-0.5$ , this negative velocity potential anomaly is strongest with one peak over the central Indian Ocean in the reanalysis data and two peaks over the central Indian Ocean and the west Pacific warm pool in the model. The center of negative velocity potential anomaly is located farther northeastward at pentad  $+1.5$ , coinciding with the propagation of the precipitation in Fig. 3. In the NCEP data, pentad  $+3.5$  lags about one pentad behind pentad  $-4.5$ .

The composites are in close resemblance to an unfiltered analysis in Fig. 10 of Higgins and Shi (2001). In the simulation, pentad  $+3.5$  resembles pentad  $-4.5$ , only with slightly less amplitude. This relatively weak signal in pentad  $+3.5$  is related to the weak equatorial heating from precipitation, as seen in Fig. 3. The relatively slow peak in the wavenumber–frequency spectrum in Fig. 1 is not captured in this composite analysis. In general, the simulated scales of the ISO signal are smaller than observed over the Indian Ocean and the strongest variability is shifted eastward. However, the study by Waliser et al. (2003a) showed that most analyzed GCMs produce a less realistic ISO pattern. A realistic precipitation pattern over the Indian Ocean is crucial for the prediction of the Indian summer mon-

soon. Although ECHAM5 fails to reproduce the ISO amplitude over certain areas, the simulated ISO period and thus the period of active and break events of the Indian summer monsoon is relatively well captured.

The three strongest ISO events are defined by root-mean-square averaged amplitudes of four consecutive maxima and minima in the principal component time series of the first two EEOFs (Fig. 5). They are marked as numbers 1 to 3 in Figs. 5a and 5b. The maxima and minima of both time series provide four phases of each selected ISO event. These four phases are in quadrature to each other. The middays of the respective pentads are used as starting dates for perturbation experiments since the predictability might be different depending on the phase of the ISO.

The strongest ISO event is found during model year 6. The maximum (minimum) of the principal component time series for the first EEOF appears on 5 July (30 July). The maximum (minimum) for the second EEOF appears on 15 July (9 August). The maximum (minimum) amplitudes associated with the four phases of the second strongest event occur during model year 9 on 25 June, 5 July, 15 July, and 25 July. For the third strongest event, the respective dates are 11 June, 21

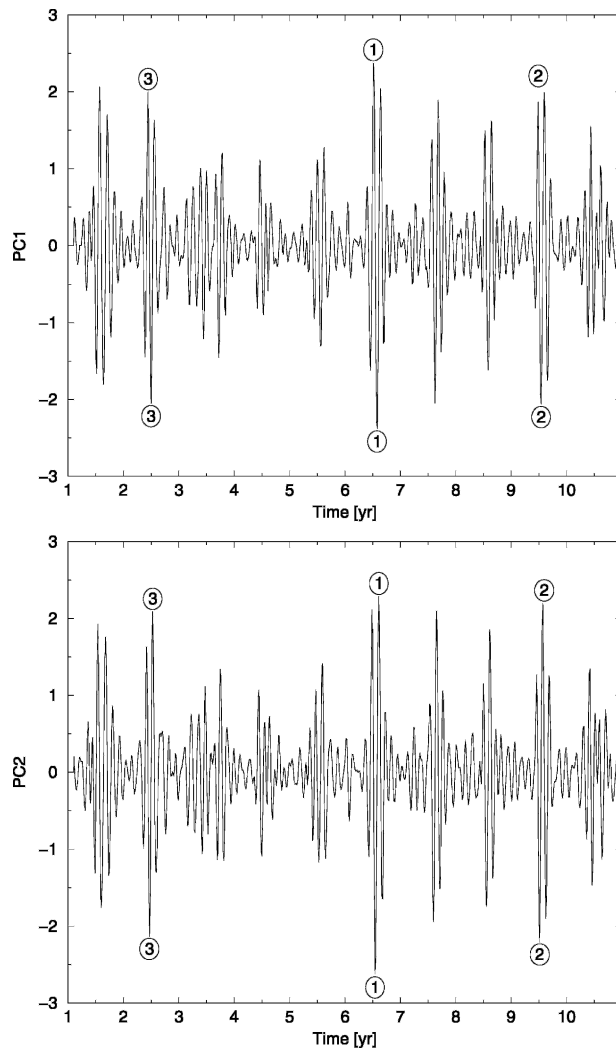


FIG. 5. Time series of (top) first and (bottom) second principal component of the respective EOFs for ECHAM5 precipitation.

June, 1 July, and 11 July of model year 2. The four consecutive phases of each event are referred to as phase 1 to phase 4 in this text. Fourteen ensemble experiments are integrated for each of these dates. To provide optimum initial conditions for those perturbation experiments, the breeding method (Toth and Kalnay 1993) is used. In numerical weather forecast, the advantage of the breeding method is the growth of large forecast uncertainties and the damping of small uncertainties. The fast-growing modes obtained by breeding are known as bred vectors and are essentially the finite-time, nonlinear extension of local Lyapunov vectors (Toth and Kalnay 1993; Cai et al. 2003). The breeding method requires a short model integration with an arbitrary initial perturbation. In the present study, this perturbation is 10% of the daily variability of

the unfiltered prognostic variables during July of the year of the detected ISO since most variability of the simulated Northern Hemisphere summer ISO occurs during July. The 14 initial perturbations for one specific date are obtained by adding or subtracting the above 10% of the daily variability of the prognostic variables during July to the initial conditions of each of the seven days between three days before and after the detected ISO maximum. For instance, the first (last) seven different initial conditions for the first phase of the strongest event are created by selecting the initial conditions for 2 to 8 July and adding (subtracting) 10% of the daily variability of the prognostic variables during July of year 6. The date of these initial conditions is then set to the given forecast date, in this example to 5 July.

The perturbed initial conditions are expected to create simulations that differ from the control experiment based on the fastest growing modes of the dynamical system. This growth will be limited by a saturation level due to the presence of nonlinear effects, which are responsible for the stability of the dynamical system. The application of the breeding method requires a short model integration, that is, one breeding cycle, after which the prognostic variables have to be scaled down to the order of a rescaling mask. In the present case the rescaling mask is defined as the amplitude of 10% of the daily variability (in terms of the standard deviation) of the prognostic variables during July of the year of the detected ISO. Cai et al. (2003) tested several rescaling factors for the ENSO variability and found promising results with a rescaling of 10% of the model variability. However, they concluded that values between 1% and 20% could be used instead without a large difference in the results.

The difference of the initial rescaling mask and the amplitude  $S$  at the end of the breeding cycle  $\tau$  is called the bred vector of the corresponding breeding cycle. The perturbation resulting from the rescaling is added to the control experiment at the new time step and the model is again integrated for a short time. Toth and Kalnay (1993) and Cai et al. (2003) assumed that an ideal perturbation is reached after four iterations. Then the final perturbation is nearly independent of the initial perturbation at the time step four integrations ago. The bred vectors increase with time to demonstrate the breeding toward the fastest growing modes. In the present case,  $\tau$  is chosen to be one pentad to detect the modes that grow fastest on the intraseasonal time scale without being influenced too strongly by higher-frequency weather modes. In numerical weather forecast, the breeding cycle  $\tau$  is only 6 h (Toth and Kalnay 1993) and for ENSO predictions Cai et al. (2003) used  $\tau$  equal to three months. The perturbation amplitude  $S$

TABLE 1. Variance of precipitation and 200-hPa zonal wind over the 14 bred vectors of the first case at the starting dates of the four phases and 10 days before the first forecast. The values are calculated before and after downscaling and then averaged over the region 25°N–25°S, 60°E–180°.

	Rescaling	Day –10	Phase 1	Phase 2	Phase 3	Phase 4
Precipitation (mm <sup>2</sup> day <sup>-2</sup> )	Before	8.430	9.066	5.244	8.584	5.123
	After	1.182	1.253	1.201	1.259	1.166
200-hPa zonal wind (m <sup>2</sup> s <sup>-2</sup> )	Before	9.412	8.468	6.044	9.881	8.465
	After	0.635	0.684	0.597	0.729	0.746

is defined by the L2 norm, as described in Eq. (1) in Cai et al. (2003) and repeated below in Eq. (1):

$$S = \frac{\sqrt{\sum_{i=1}^n \left[ \frac{\int (V_i^p - V_i^c)^2 dx dy}{\sigma_i^2} \right]}}{\sqrt{n}}. \quad (1)$$

Here  $V_i$  is one of the prognostic variables: vorticity, divergence, temperature, specific humidity, or surface pressure, used to determine  $S$ . Each of the 31 vertical levels is treated as a different variable so that  $n$  is equal to 125. The values of perturbed experiments are denoted by  $p$  and the ones of the control simulation by  $c$ ;  $\sigma_i$  represents the standard deviation of the corresponding unfiltered variable. The horizontal integration in  $xy$  directions is performed over the global model domain.

The scaling factor that leads to the initial conditions for one ensemble member is determined from the rescaling mask. At the beginning of each forecast day, the values for  $S$  are calculated according to Eq. (1). After five days, the perturbation is scaled down to the scaling factor. The fifth iteration is the beginning of the perturbed forecast for the first ISO phase. The initializations of the other three phases are obtained by a continuation of the breeding method. Most ensembles indicate a slightly decreased size of the bred vectors after the first breeding cycle and a nearly constant growth rate afterwards. This is in contrast to the increase in growth rate as theoretically expected. A modification to the breeding method is discussed in section 4. This change leads to the expected increase in the growth rate.

Table 1 describes the variance of precipitation and 200-hPa zonal wind over the 14 bred vectors of the first case at the starting dates of the four phases and 10 days before the first forecast. Averaged over the region 25°N to 25°S, 60°E to 180° the values barely increase as a result of the breeding method as it is used in the present study. Prior to downscaling, the strongest variance occurs during phases 1 and 3, which are identified by the first EEOF. The variances during phases 2 and 4 (iden-

tified by the second EEOF) are slightly lower. However, these variances show virtually no difference to the variances 10 days before the first forecast experiments. After downscaling, the variances indicate even less difference between the different phases. The spatial distribution of variances over the region specified above also reveals no significant changes in the variance in precipitation and 200-hPa zonal wind (not shown). This shows that the breeding method as it is used in the present study does not significantly improve the initial conditions.

The obtained initial conditions are used to produce 90-day forecasts for all ensemble members. Since the current study only provides insight into the simulated ISO as opposed to the observed ISO, only the theoretical or potential predictability can be calculated. Additionally, it is assumed that ISO predictability is strongest for strong events; hence assessing predictability of the three strongest ISO events in the time series results in the upper limit of ISO predictability.

### 3. Results

Two different approaches are applied to identify the ISO signal in the ensemble forecasts. In the first approach, the forecasts are appended to the previous 120 days of the control experiment. In accordance with Walliser et al. (2003c), a 40-day triangular taper is applied to either end of the resulting 210-day time series in order to be able to bandpass filter the data with the 30–90-day Lanczos filter. However, although time filtering is widely used to examine the ISO signal, this approach is worrisome for predictability studies since predictability can be overestimated. In the second approach, the upper limit of ISO predictability is investigated using daily averaged anomalies, reconstructed from a projection on the first four EOFs of Northern Hemisphere summer data from the 10-yr control simulation. Wheeler and Hendon (2004) used a similar method by projecting daily data on the first two EOFs. Figure 6 shows the first four EOFs for precipitation. These EOFs reflect the eastward and northward propagating ISO pattern described in Fig. 3.

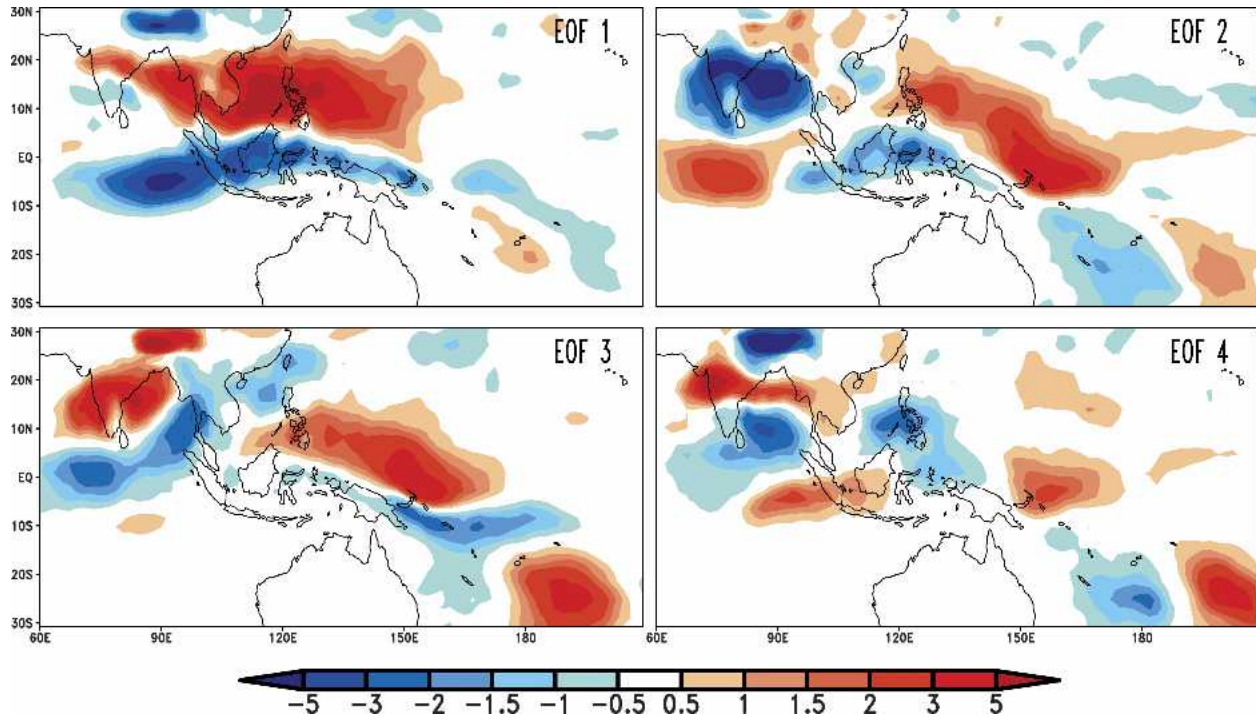


FIG. 6. Empirical orthogonal functions 1 through 4 for ECHAM5 precipitation.

In the first approach, precipitation and 200-hPa velocity potential are analyzed to compare the present results to a previous study by Waliser et al. (2003c). In the second approach, 200-hPa zonal wind is additionally analyzed since it is a measurable and, therefore, a more direct and useful variable for climate predictions. To avoid a too strong influence of the subtropical jet streams, the EOFs for 200-hPa zonal wind are confined between 20°N and 20°S. Figures 7 and 8 depict time series for all ensemble members in the first phase of the strongest case averaged over the region 10°–20°N, 90°–120°E, which roughly corresponds to Southeast Asia (see box in Fig. 11). The thin lines show each one of the 15 ensemble members including the control experiment and the thick line represents the mean of all members. Day zero indicates the start of the forecast experiments. Due to bandpass filtering, the forecast error is nonzero at forecast day zero in Fig. 7. Since the ISO signals of each member diverge with increasing time, the amplitude of the mean signal decreases, indicating less predictability with time. However, the 30–60-day period is still detectable after 60 forecast days. For a more quantitative approach of the predictability, the signal-to-noise ratio of the forecast experiments is obtained according to Waliser et al. (2003c). This enables a more direct comparison to their results. The signal  $\sigma_s$  for one phase  $\phi$  of one case  $k$  is obtained at a given forecast day  $j$  by calculating the variance  $\sigma_{s_{\phi k j}}$  within a sliding win-

dow  $t$  ranging from  $-L$  days to  $+L$  days [Eq. (2)];  $L$  is predefined as 25 days, hence the sliding window contains approximately one complete ISO cycle;  $X$  represents the geophysical quantity that is analyzed. The superscript 0 indicates the control experiment:

$$\sigma_{s_{\phi k j}} = \frac{1}{2L + 1} \sum_{t=-L}^L (X_{\phi, k, j+t}^0)^2. \quad (2)$$

The corresponding noise  $\sigma_e$  at a given forecast day  $j$ , also known as the forecast error relative to the control experiment, is averaged over the 14 ensemble members  $m$  for one phase  $\phi$  of one case  $k$ . It is defined as

$$\sigma_{e_{\phi k j}} = \frac{1}{14} \sum_{m=1}^{14} (X_{\phi, k, j}^m - X_{\phi, k, j}^0)^2. \quad (3)$$

Figures 9 and 10 show the mean signal and noise averaged over all four phases  $\phi$  of all three cases  $k$  over the same region as in Figs. 7 and 8. Considering a signal-to-noise ratio of one as a limit for useful predictability, the average predictability of bandpass-filtered precipitation (200-hPa velocity potential) is limited to 28 (36) days with the 95% confidence interval starting at 25 (33) days. Using the more appropriate projection on EOFs, the average predictability is reduced to 27 days for precipitation and 23 days for 200-hPa velocity potential. The 200-hPa zonal wind is still predictable for about 33 days. The 95% confidence interval starts

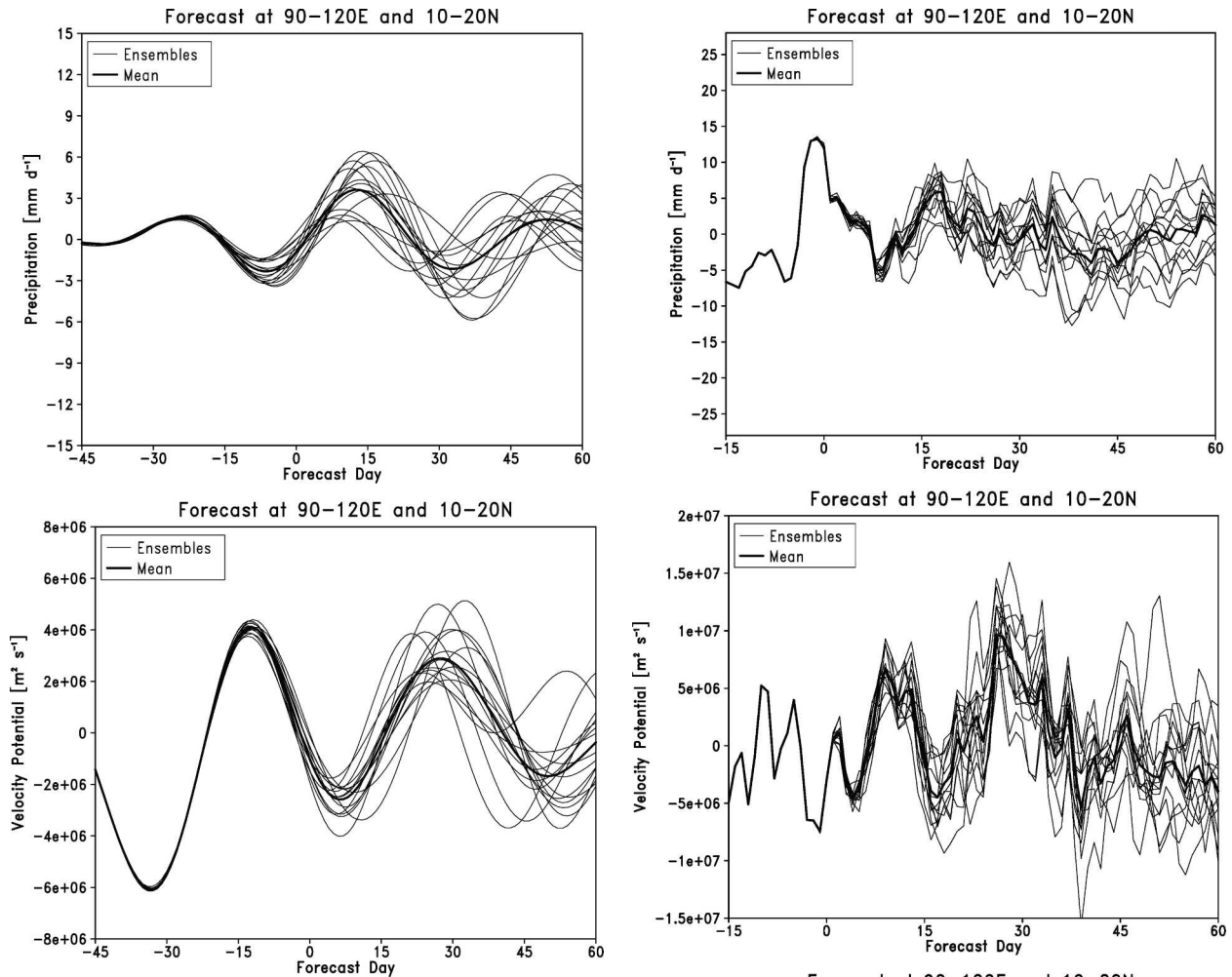


FIG. 7. Error growth of (top) 30–90-day filtered precipitation and (bottom) 200-hPa velocity potential predictions for phase 1 in case 1. Values are averaged over the region 10°–20°N, 90°–120°E.

about one day earlier for all three variables. This shows the lower variability of the ensembles when only the first four EOFs are considered. The 95% confidence interval is calculated with a Student's *t* test.

The left panels of Fig. 11 show maps of the variance of the composites for precipitation, 200-hPa velocity potential and 200-hPa zonal wind as they are depicted in Figs. 3, 4 and 14. The right panels show, for each grid point, the lead time at which a signal-to-noise ratio of one or lower is reached for EOF-projected data. These lead times provide further insight into the spatial distribution of the ISO predictability. High lead times indicate a high predictability of the simulated ISO. Areas with strong variance, and therefore strong signals, are not necessarily areas with high lead times. Over the equator, high lead times of more than 30 days can be found up to 30° east of the strongest variance, espe-

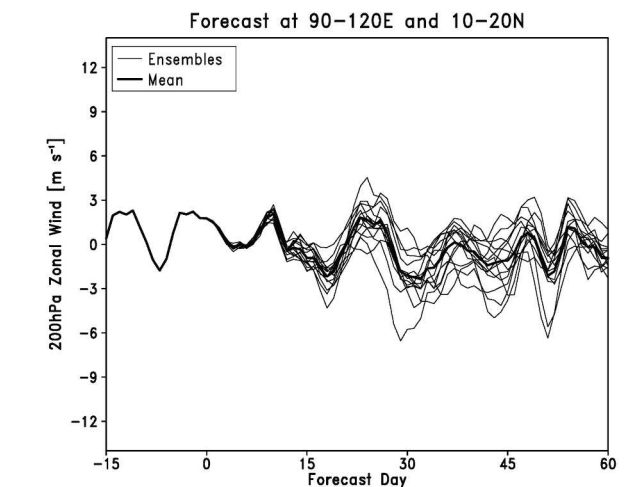


FIG. 8. As in Fig. 7 but for (top) EOF-projected precipitation, (middle) 200-hPa velocity potential, and (bottom) 200-hPa zonal wind predictions.

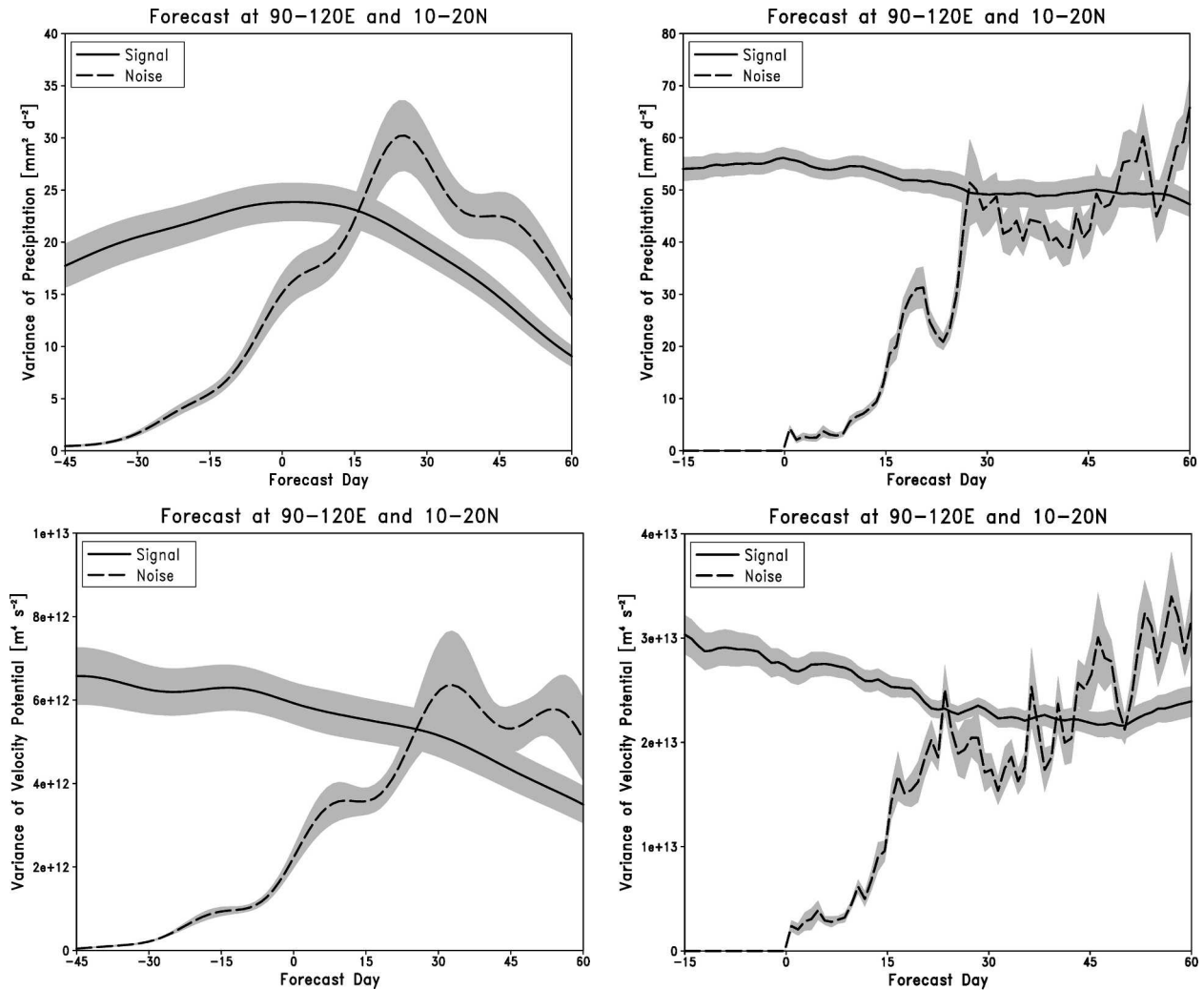


FIG. 9. Signal-to-noise ratio of (top) bandpass-filtered precipitation and (bottom) 200-hPa velocity potential predictions averaged over all four phases in all three cases. Shading represents the significance at the 95% interval for all 12 forecasts. All values are averaged over the region  $10^{\circ}$ – $20^{\circ}$ N,  $90^{\circ}$ – $120^{\circ}$ E.

cially for precipitation and 200-hPa zonal wind over the Maritime Continent and the central Pacific where the effect of the eastward propagating ISO is strongest. Also farther away from the equator, lead times can be highest to the east of the strongest variance, as over the South China Sea and the west Pacific warm pool. For precipitation, the long lead time is extended to the eastern Indian Ocean, whereas long lead times of 200-hPa zonal wind can be found over the western Indian Ocean and over most of the west and central Pacific. Additionally, a long lead time for prediction of 200-hPa zonal wind is found near the South Pacific convergence zone (SPCZ) (Vincent 1994) at about  $15^{\circ}$ S near the date line. Matthews et al. (1996) proposed that subtropical

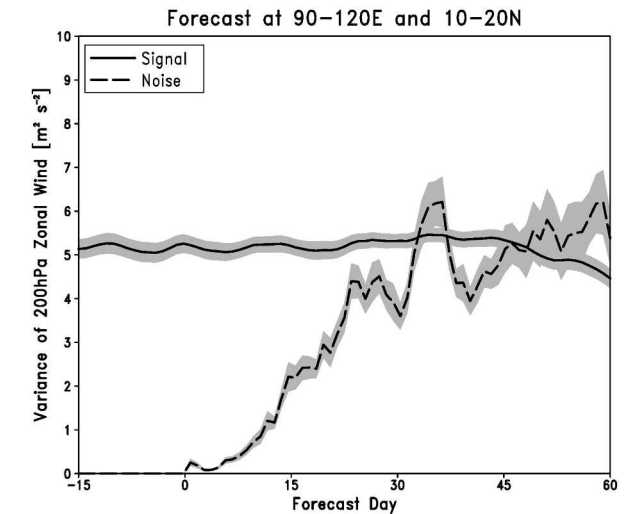


FIG. 10. As in Fig. 9 but for (top) EOF-projected precipitation, (middle) 200-hPa velocity potential, and (bottom) 200-hPa zonal wind predictions.

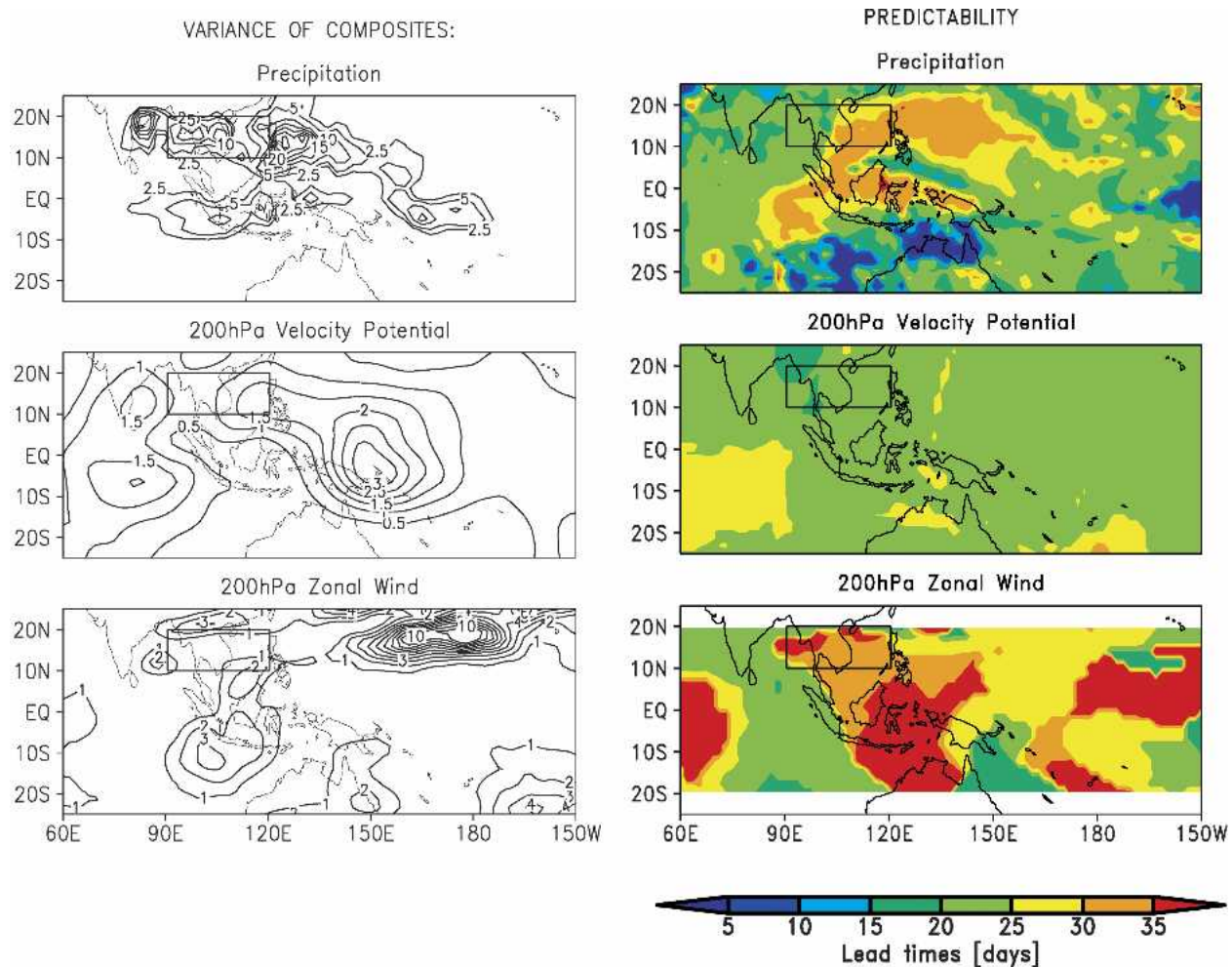


FIG. 11. Variance of composites from (left) Figs. 3, 4, and 14 and number of forecast days until (right) the signal equals the noise for (top) precipitation, (middle) 200-hPa velocity potential, and (bottom) 200-hPa zonal wind.

Rossby wave propagation associated with the ISO accounts for the poleward and eastward extension of convection along the SPCZ. The forecast of 200-hPa velocity potential is rather uniformly distributed and much lower in the EOF-projected signal than in the bandpass-filtered signal (not shown). The area between 10°–20°N, 90°–120°E, which is analyzed in Figs. 7–10, is marked by a black rectangular box.

Figure 12 shows the predictability of precipitation during the four different phases of the ISO. The initial conditions for the four consecutive phases 1 to 4 have similar horizontal patterns to the composited pentads –0.5, +1.5, +3.5, and –2.5 in the right side of Fig. 3. The third phase also corresponds to pentad –4.5. In general, the strength of predictability resembles the signal of precipitation with high values over the northern summer ITCZ and the SPCZ. The strongest predictability is found in phase 2 at the end of the convective

ISO phase and during the active Indian summer monsoon. Predictability decreases during phases 3 and 4. It is lowest during phase 1, at the beginning of the convective phase. In phases 2 and 3 the predictability reaches more than 30 days over the South China Sea, the west Pacific warm pool and most parts of the Maritime Continent. Over the west Pacific warm pool, it shifts slightly northward from phase 2 to 3, following the northward propagation of deep convection. Although predictability decreases in general during phases 4 and 1, values of more than 20 days can still be found. Over the eastern Indian Ocean, predictability even increases, confirming a stronger predictability of an upcoming dry phase than an upcoming convective phase. The predictability over southern India is lower but still reaches more than 15 days during all four phases.

The predictability of 200-hPa velocity potential (Fig.

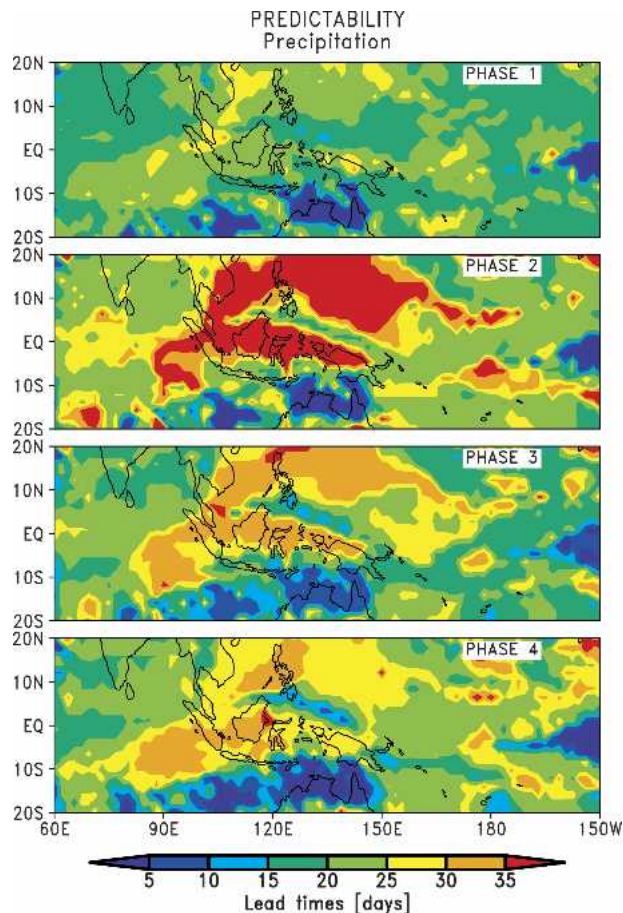


FIG. 12. Number of forecast days until the signal equals the noise for precipitation. See text for more explanation about how the four phases of the oscillation are defined.

13) reaches high values over the Maritime Continent in phases 2 and 3. Strong predictability shifts from the Maritime Continent to the central Indian Ocean and the SPCZ in phases 3 and 4. In phase one it shifts back to the Maritime Continent. However, in addition to not being a directly measurable variable, the broad scale of velocity potential makes it a less useful variable for climate predictions. Figure 14 shows the composites of 200-hPa zonal wind, analogous to Figs. 3 and 4, as well as the corresponding predictability for each phase. As with precipitation and 200-hPa velocity potential, the strongest predictability is found over the Maritime Continent and the central Pacific during phase 2. During phase 3, predictability decreases over these regions but increases over the west Pacific warm pool. In phases 4 and 1, predictability decreases and extends farther eastward. It shifts northward following the region of low anomalies. Analogous to precipitation, strong predictability occurs during low anomalies and easterlies, related to the end of the convective phase. Over the

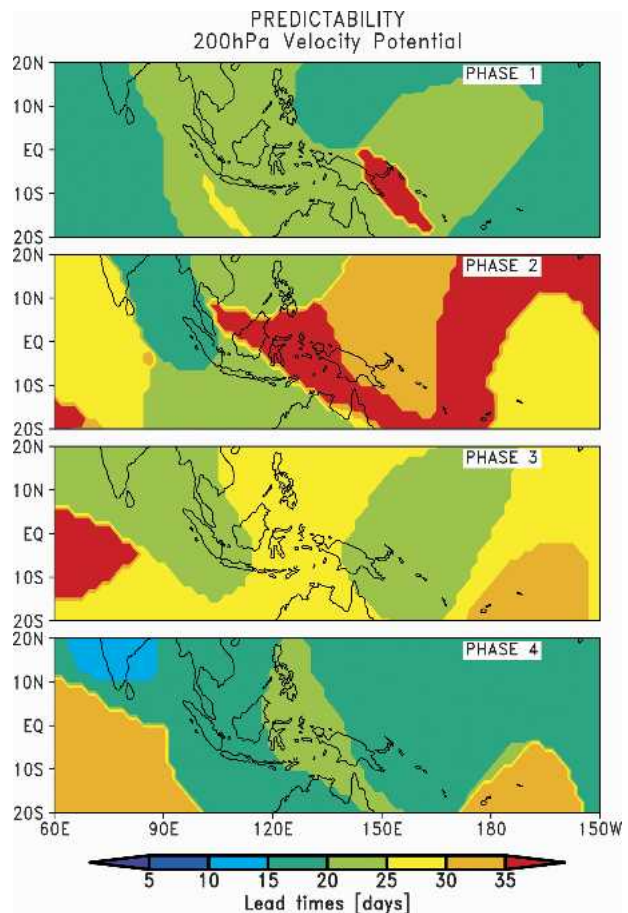


FIG. 13. As in Fig. 12 but for 200-hPa velocity potential.

Indian Ocean, predictability is in general lower than downstream of strong ISO activity. However, during phases 1 and 2, predictability still reaches more than 20 days over India. Although the location of long lead times changes slightly with the ISO phase, the predictability is in general highest over areas with a strong ISO signal. This strong signal reveals a potential for an improvement in intraseasonal prediction over the associated areas and by this an improvement of the prediction of the active and break phases of the Asian summer monsoon.

In regards to the breeding method, it should be noted that contrary to what is expected and desired, the breeding method as used in this study did not significantly increase the intraensemble variability of the initial condition perturbations with time. To test the sensitivity of the results to this characteristic, additional breeding cycles were calculated. To focus on tropical motions, the vorticity is omitted from Eq. (1). The first bred vector reaches a forecast value  $S$  of 17.5 and the forecast value increases with each iteration. After four iterations, a saturation value is reached as proposed by Toth and Kalnay (1993). In the shown test calculation

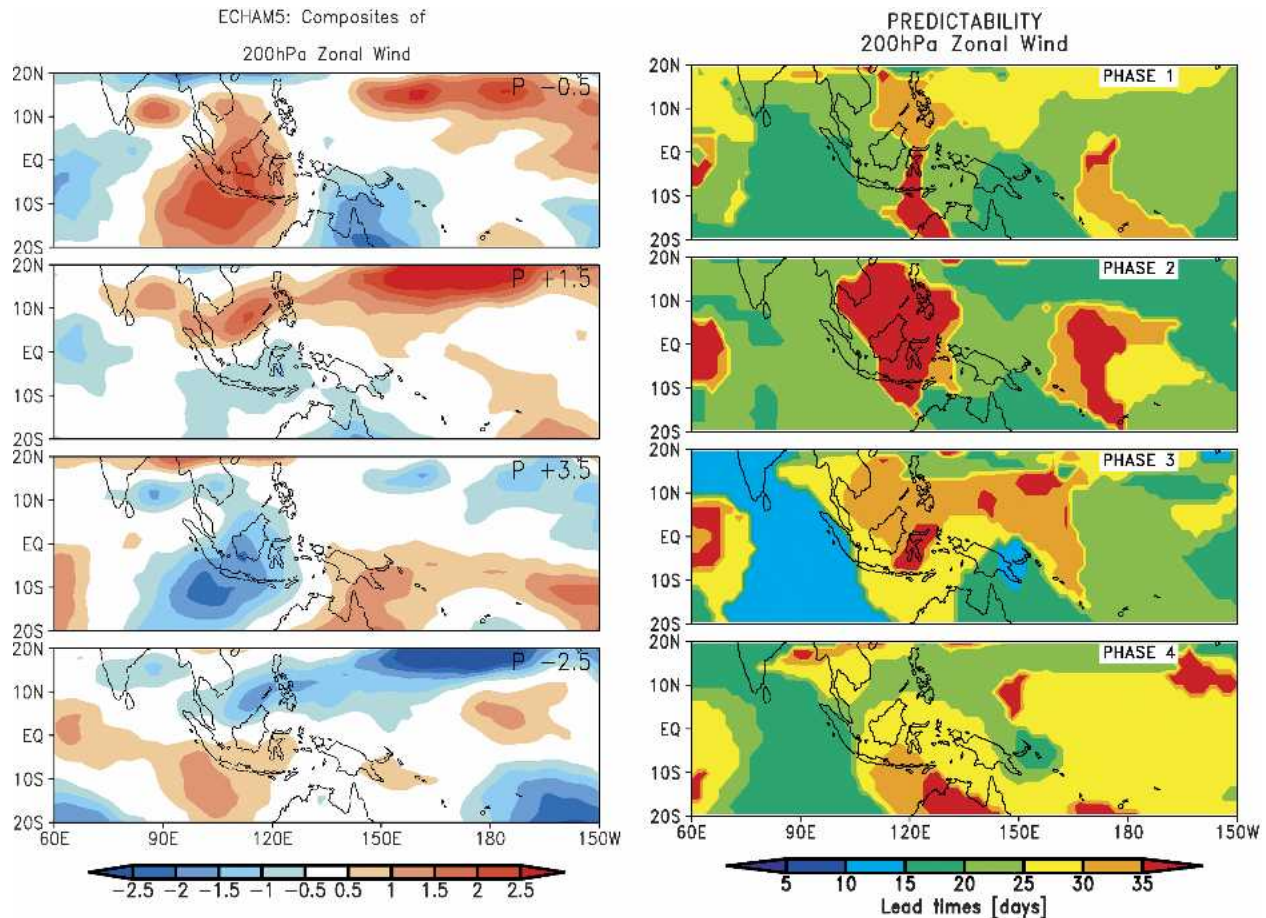


FIG. 14. (left) Composites of 200-hPa zonal wind ( $m s^{-1}$ ). (right) Forecast days as in Fig. 12 but for 200-hPa zonal wind.

the saturation value ranges from 36 to 42, whereas the saturation value in the initial use of the breeding method reaches only values around 17. Figure 15 shows results of one 14-member ensemble forecast, created with 1) the breeding method originally used in this study and 2) with the modified approach described above. The modified approach results in an expected decrease in potential predictability due to the inclusion of a larger model uncertainty. However, although the predictability of 200-hPa zonal wind decreases from more than 30 days to less than 10 days over the previously analyzed region in Southeast Asia, this example shows no decrease of predictability for precipitation. The results for precipitation obtained from the originally used breeding method are still within the 95% confidence interval of a *t* test over all 14 ensemble members.

#### 4. Conclusions

This study revisits the predictability of the northern summer ISO (see, e.g., Waliser et al. 2003c) using the

ECHAM5 atmospheric GCM. ECHAM5 was chosen because it exhibits a relatively realistic ISO as well as more realistic precipitation variability over the Indian Ocean compared with earlier models used to study the ISO. In addition, the model was run at relatively high resolution (T63 and 31 layers up to a height of 10 hPa in the vertical). A further difference from previous studies is that we initialize the runs using a breeding method (Toth and Kalnay 1993) designed to better capture the fastest growing disturbances.

The ensemble forecasts in Waliser et al. (2003c) were initialized with random perturbations. They found the limit of predictability for bandpass-filtered data at about 15 days for precipitation and about 25 days for 200-hPa velocity potential over an area covering India and Southeast Asia. The present study shows that bandpass filtering leads to an overestimation of predictability compared to projecting the forecasts on the first four EOFs. This study focuses on the three strongest ISO cases and detects an upper limit of predictability of more than 15 (20) days over India and more than

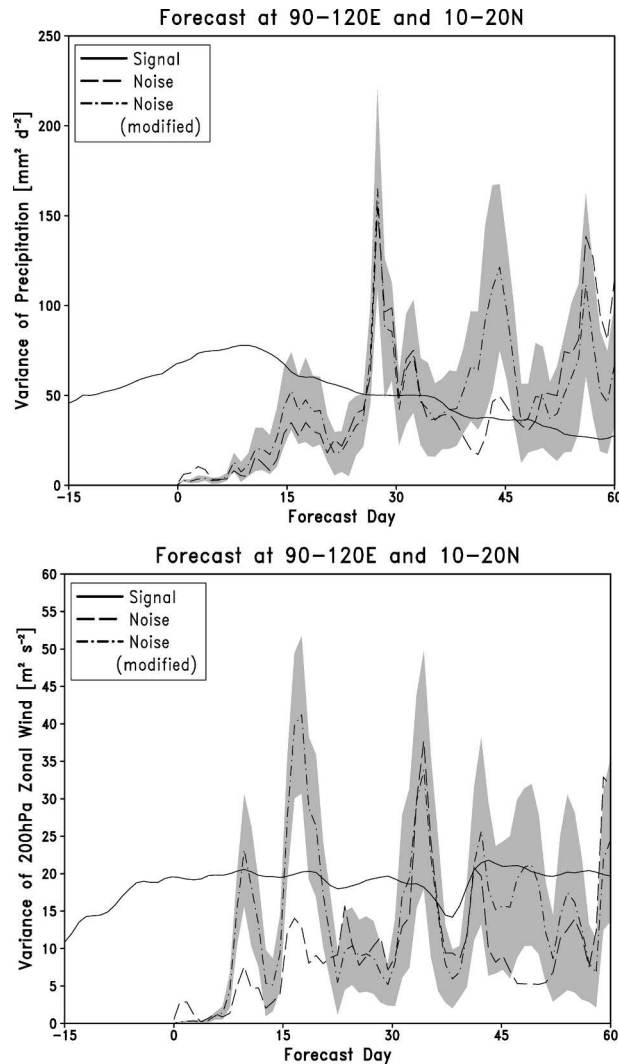


FIG. 15. (top) Signal-to-noise ratios of EOF-projected precipitation and (bottom) 200-hPa zonal wind predictions for the first phase in the second case. The modified noise is obtained from the 14 forecast experiments with vorticity omitted in the calculation for initial conditions. Shading represents the significance at the 95% interval for the 14 ensembles of the modified noise. All values are averaged over the region  $10^{\circ}$ – $20^{\circ}$ N,  $90^{\circ}$ – $120^{\circ}$ E.

20 (30) days over Southeast Asia for precipitation (200-hPa zonal wind), as shown in Fig. 11. It is suggested that the restriction to the three strongest ISO cases in the present study is responsible for the increase in predictability since the inclusion of weaker ISO events is expected to decrease the signal of the intraseasonal variability (Waliser et al. 2003b,c). For the above reason, the current results provide the upper limit of predictability. Over parts of Southeast Asia, the predictability reaches about 27 days for precipitation and about 33 days for 200-hPa zonal wind (see Figs. 10 and 11). Re-

sults for 200-hPa velocity potential reveal a uniform predictability of more than 20 days over the analyzed regions, but these results should be treated with caution since velocity potential is not measurable and thus a more indirect variable.

The spatial analysis of different phases of the ISO reveals that the predictability follows the eastward and northward propagating ISO during the active and break phases of the monsoon. Precipitation reveals increased predictability at the end of the convective phase. Analogously, the 200-hPa zonal wind shows strongest predictability during low and easterly anomalies. Owing to the long lead time in the upper limit of theoretical predictability, there appears to be untapped predictability for the propagation of the ISO and hence the evolution of the subsequent monsoon phase, either the active or the break phase. The present study provides detailed maps of areas with high potential predictability within the intraseasonal time scale. Although different areas are favored during different phases of the monsoon, the regions in South Asia most affected by the monsoon reveal strong potential predictability during all four phases. Hence the present study motivates further improvements in the simulation and forecast on the intraseasonal time scale.

As with all results obtained by numerical simulations, caution is warranted. The systematic model errors as described in Figs. 1–4 have been neglected in the current study. Hence the current study is only a broad estimate for the upper limit of predictability of observed intraseasonal variability. Waliser et al. (1999b) showed that a coupling of the atmospheric GCM to a mixed layer model could lead to a more realistic simulation of the ISO compared to the use of climatological SSTs as in the present study. Hence the exclusion of SST coupling may lead to an underestimation of the predictability. A future study will utilize an atmospheric GCM coupled to a mixed layer ocean model and the predictability will be studied with observed initial conditions.

*Acknowledgments.* The authors thank Eugenia Kalnay, Ming Cai, Zoltan Toth, and Mozheng Wei for helpful comments regarding the breeding method. Comments of Harry Hendon and two anonymous reviewers helped to improve the manuscript and were highly appreciated. The CMAP observations and the NCEP reanalysis data were kindly provided by the Climate Prediction Center. This study was supported by the National Oceanographic and Atmospheric Administration under Grant NA16GP2021 and the National Science Foundation under Grant ATM-0094416.

## REFERENCES

- Barnston, A. G., and Coauthors, 1994: Long-lead seasonal forecasts—Where do we stand? *Bull. Amer. Meteor. Soc.*, **75**, 2097–2114.
- , Y. He, and M. H. Glantz, 1999: Predictive skill of statistical and dynamical climate models in SST forecasts during the 1997–98 El Niño episode and the 1998 La Niña onset. *Bull. Amer. Meteor. Soc.*, **80**, 217–244.
- Cai, M., E. Kalnay, and Z. Toth, 2003: Bred vectors of the Zebiak–Cane model and their potential application to ENSO predictions. *J. Climate*, **16**, 40–56.
- Cane, M., S. E. Zebiak, and S. C. Dolan, 1986: Experimental forecasts of El Niño. *Nature*, **321**, 827–832.
- Chen, T.-C., and J. C. Alpert, 1990: Systematic errors in the annual and intraseasonal variations of the planetary-scale divergent circulation in NMC medium-range forecasts. *Mon. Wea. Rev.*, **118**, 2607–2623.
- DelSole, T., and J. Shukla, 2002: Linear prediction of Indian monsoon rainfall. *J. Climate*, **15**, 3645–3658.
- Duchon, C. E., 1979: Lanczos filtering in one and two dimensions. *J. Appl. Meteor.*, **18**, 1016–1022.
- Ferranti, L., T. N. Palmer, F. Molteni, and E. Klinker, 1990: Tropical–extratropical interaction associated with the 30–60 day oscillation and its impact on medium and extended range prediction. *J. Atmos. Sci.*, **47**, 2177–2199.
- Graham, N., and T. P. Barnett, 1995: ENSO and ENSO-related predictability. Part II: Northern Hemisphere 700-mb height predictions based on a hybrid coupled ENSO model. *J. Climate*, **8**, 544–549.
- Hayashi, Y.-Y., 1981: Space–time cross spectral analysis using the maximum entropy method. *J. Meteor. Soc. Japan*, **59**, 620–624.
- Hendon, H. H., and B. Liebmann, 1990a: A composite study of onset of the Australian summer monsoon. *J. Atmos. Sci.*, **47**, 2227–2240.
- , and —, 1990b: The intraseasonal (30–50 day) oscillation of the Australian summer monsoon. *J. Atmos. Sci.*, **47**, 2909–2923.
- , —, and J. D. Glick, 1998: Oceanic Kelvin waves and the Madden–Julian oscillation. *J. Atmos. Sci.*, **55**, 88–101.
- , —, M. Newman, J. D. Glick, and J. E. Schemm, 2000: Medium-range forecast errors associated with active episodes of the Madden–Julian oscillation. *Mon. Wea. Rev.*, **128**, 69–86.
- Higgins, R. W., and W. Shi, 2001: Intercomparison of the principal modes of interannual and intraseasonal variability of the North American monsoon system. *J. Climate*, **14**, 403–417.
- , J.-K. E. Schemm, W. Shi, and A. Leetmaa, 2000: Extreme precipitation events in the western United States related to tropical forcing. *J. Climate*, **13**, 793–820.
- Inness, P. M., J. M. Slingo, S. J. Woolnough, R. B. Neale, and V. D. Pope, 2001: Organization of tropical convection in a GCM with varying vertical resolution: Implications for the simulation of the Madden–Julian oscillation. *Climate Dyn.*, **17**, 777–793.
- Jones, C., 2000: Occurrence of extreme precipitation events in California and relationships with the Madden–Julian oscillation. *J. Climate*, **13**, 3576–3587.
- , D. E. Waliser, J. E. Schemm, and W. K. Lau, 2000: Prediction skill of the Madden and Julian oscillation in dynamical extended range weather forecasts. *Climate Dyn.*, **16**, 273–289.
- Kang, I.-S., and Coauthors, 2002: Intercomparison of the climatological variations of Asian summer monsoon precipitation simulated by 10 GCMs. *Climate Dyn.*, **19**, 383–395.
- Kemball-Cook, S. R., B. Wang, and X. Fu, 2002: Simulation of the intraseasonal oscillation in the ECHAM-4 model: The impact of coupling with an ocean model. *J. Atmos. Sci.*, **59**, 1433–1453.
- Kessler, W. S., and R. Kleeman, 2000: Rectification of the Madden–Julian oscillation into the ENSO cycle. *J. Climate*, **13**, 3560–3575.
- , M. McPhaden, and K. M. Weickmann, 1995: Forcing of intraseasonal Kelvin waves in the equatorial Pacific. *J. Geophys. Res.*, **100**, 10 613–10 631.
- Lau, K.-M., H.-T. Wu, and S. Yang, 1998: Hydrologic processes associated with the first transition of the Asian summer monsoon: A pilot satellite study. *Bull. Amer. Meteor. Soc.*, **79**, 1871–1882.
- LieSS, S., and L. Bengtsson, 2004: The intraseasonal oscillation in ECHAM4. Part II: Sensitivity studies. *Climate Dyn.*, **22**, 671–688.
- Lin, X., and R. H. Johnson, 1996: Kinematic and thermodynamic characteristics of the flow over the western Pacific warm pool during TOGA COARE. *J. Atmos. Sci.*, **53**, 695–715.
- Lorenz, E. N., 1965: A study of the predictability of a 28-variable atmospheric model. *Tellus*, **17**, 321–333.
- , 1982: Atmospheric predictability experiments with a large numerical model. *Tellus*, **34**, 505–513.
- Madden, R. A., and P. R. Julian, 1994: Observations of the 40–50-day tropical oscillation—A review. *Mon. Wea. Rev.*, **122**, 814–837.
- Maloney, E. D., and D. L. Hartmann, 2000: Modulation of eastern North Pacific hurricanes by the Madden–Julian oscillation. *J. Climate*, **13**, 1451–1460.
- Matthews, A. J., B. J. Hoskins, J. M. Slingo, and M. Blackburn, 1996: Development of convection along the SPCZ within a Madden–Julian oscillation. *Quart. J. Roy. Meteor. Soc.*, **122**, 669–688.
- McPhaden, M. J., and B. A. Taft, 1988: Dynamics of seasonal and intraseasonal variability in the eastern equatorial Pacific. *J. Phys. Oceanogr.*, **18**, 1713–1732.
- Mo, K. C., 2001: Adaptive filtering and prediction of intraseasonal oscillations. *Mon. Wea. Rev.*, **129**, 802–817.
- , and R. W. Higgins, 1998a: Tropical convection and precipitation regimes in the western United States. *J. Climate*, **11**, 2404–2423.
- , and —, 1998b: Tropical influences on California precipitation. *J. Climate*, **11**, 412–430.
- Paegle, J. N., L. A. Byerle, and K. C. Mo, 2000: Intraseasonal modulation of South American summer precipitation. *Mon. Wea. Rev.*, **128**, 837–850.
- Raymond, D. J., 2000: The Hadley circulation as a radiative–convective instability. *J. Atmos. Sci.*, **57**, 1286–1297.
- Roeckner, E., and Coauthors, 2003: The atmospheric general circulation model ECHAM5. Part I: Model description. Max-Planck-Institut für Meteorologie Rep. 349, Hamburg, Germany, 140 pp.
- Slingo, J. M., and Coauthors, 1996: Intraseasonal oscillations in 15 atmospheric general circulation models: Results from an AMIP diagnostic subproject. *Climate Dyn.*, **12**, 325–357.
- Sperber, K. R., and Coauthors, 2001: Dynamical seasonal predictability of the Asian summer monsoon. *Mon. Wea. Rev.*, **129**, 2226–2248.
- Tompkins, A. M., 2002: A prognostic parameterization for the subgrid-scale variability of water vapor and clouds in large-

- scale models and its use to diagnose cloud cover. *J. Atmos. Sci.*, **59**, 1917–1942.
- Toth, Z., and E. Kalnay, 1993: Ensemble forecasting at NMC: The generation of perturbations. *Bull. Amer. Meteor. Soc.*, **74**, 2317–2330.
- Van den Dool, H. M., 1994: Long-range weather forecasts through numerical and empirical methods. *Dyn. Atmos. Oceans*, **20**, 247–270.
- Vincent, D. G., 1994: The South Pacific convergence zone (SPCZ): A review. *Mon. Wea. Rev.*, **122**, 1949–1970.
- Waliser, D. E., C. Jones, J.-K. E. Schemm, and N. E. Graham, 1999a: A statistical extended-range tropical forecast model based on the slow evolution of the Madden–Julian oscillation. *J. Climate*, **12**, 1918–1939.
- , K. M. Lau, and J.-H. Kim, 1999b: The influence of coupled sea surface temperatures on the Madden–Julian oscillation: A model perturbation experiment. *J. Atmos. Sci.*, **56**, 333–358.
- , and Coauthors, 2003a: AGCM simulations of intraseasonal variability associated with the Asian summer monsoon. *Climate Dyn.*, **21**, 423–446.
- , K. M. Lau, W. Stern, and C. Jones, 2003b: Potential predictability of the Madden–Julian oscillation. *Bull. Amer. Meteor. Soc.*, **84**, 33–50.
- , W. Stern, S. Schubert, and K. M. Lau, 2003c: Dynamic predictability of intraseasonal variability associated with the Asian summer monsoon. *Quart. J. Roy. Meteor. Soc.*, **129**, 2897–2925.
- Wang, B., and H. Rui, 1990: Synoptic climatology of transient tropical intraseasonal convection anomalies. *Meteor. Atmos. Phys.*, **44**, 43–61.
- Weickmann, K. M., 1991: El Niño/Southern Oscillation and Madden–Julian (30–60 day) oscillations during 1981–1982. *J. Geophys. Res.*, **96**, 3187–3195.
- Wheeler, M., and K. M. Weickmann, 2001: Real-time monitoring and prediction of modes of coherent synoptic to intraseasonal tropical variability. *Mon. Wea. Rev.*, **129**, 2677–2694.
- , and H. H. Hendon, 2004: An all-season real-time multivariate MJO index: Development of an index for monitoring and prediction. *Mon. Wea. Rev.*, **132**, 1917–1932.
- Williamson, D. L., and P. J. Rasch, 1994: Water vapour transport in the NCAR CCM2. *Tellus*, **46A**, 36–51.
- Xie, P., and P. A. Arkin, 1997: A 17-year monthly analysis based on gauge observations, satellite estimates, and numerical model outputs. *Bull. Amer. Meteor. Soc.*, **78**, 2539–2558.
- Yasunari, T., 1980: A quasi-stationary appearance of 30 to 40 day period in the cloudiness fluctuations during the summer monsoon over India. *J. Meteor. Soc. Japan*, **58**, 225–229.
- , 1981: Structure of an Indian summer monsoon system with around 40-day period. *J. Meteor. Soc. Japan*, **59**, 336–354.